Electronic Supplementary Material (ESI) for Journal of Materials Chemistry A.

Supporting Information

Strong, persistent superficial oxidation-assisted chemical bonding of black phosphorus with multiwall carbon nanotube for high-capacity ultradurable storage of lithium and sodium

Safa Haghighat-Shishavan,[1] Masoud Nazarian-Samani,[1,2] Mahboobeh Nazarian-Samani,[1] Ha-Kyung Roh,[1] Kyung-Yoon Chung,[3] Byung-Won Cho,[3] Seyed Farshid Kashani-Bozorg,[2,*] Kwang-Bum Kim,[1,*]

[1]Department of Materials Science and Engineering, Yonsei University, 134 Sinchon-dong, Seodaemoon-gu, Seoul 120-749, Republic of Korea.

[2]School of Metallurgy and Materials Engineering, College of Engineering, University of Tehran, 11155-4563, Tehran, IR Iran.

[3]Center for Energy Convergence, Korea Institute of Science and Technology, Hwarang-ro, Seongbuk-gu, Seoul 02792, Republic of Korea.

*Corresponding authors: fkashani@ut.ac.ir (S.F. Kashani-Bozorg), kbkim@yonsei.ac.kr (K.-B. Kim)

S1. Experimental Section

S1.1. Materials

Commercial RP (Alfa Aesar, -100 mesh, 98.9%), MWCNT (Carbon Nanomaterial Technology Co. Ltd., Korea), PVDF (Sigma-Aldrich, Mw=534000), PAA (Sigma-Aldrich, Mv = 3000000), and NaCMC (Sigma-Aldrich, Mw = 700000) were used as received without any further purification processes.

S1.2. Synthesis of BP

In the first step, RP was placed in a stainless steel vial and sealed in a glovebox under high purity argon protection, followed by ball milling with a Fritsch P6 planetary ball mill. The ball-to-powder (BPR) mass ratio was maintained at 40:1, and the milling speed was kept at 450 rpm for periods ranging up to 60 h. Then, BP30 and BP60 samples (milled for 30 and 60 h, respectively) were selected for the second round of milling.

S1.3. Synthesis of BP-CNT composites

The milled BP30 and BP60 were mixed with MWCNTs at 7:3 weight ratio in air for 30–45 min. Then, the mixtures of air-exposed BP and CNTs were transferred into a vial inside the glovebox under argon protection to avoid excessive degradation, and milled at a BPR of 20:1 and speed of 300 rpm for 20 and 50 h to prepare the BP-CNT composites (BPC1 to BPC4). The details of milling steps are also presented in **Table 1**. **Scheme 1, approach A** illustrates the various stages in the synthesis of BP-CNT composites.

S1.4. Synthesis of control test samples

As a control test to confirm the necessity of two milling steps to reach the final BP-CNT homogeneous mixture, we also milled mixed RP and CNT in the same ratio (7:3) in one step for up to 50 h with a BPR of 40:1 and a speed of 450 rpm, as depicted in **Scheme 1, approach B**. Small amounts of powders were collected at certain time intervals to monitor the milling progress.

We also designed one extra sample without controlled air exposure to compare its structural properties and electrochemical properties (**Table 1**, BPC5). For this purpose, BP60 was carefully synthesized under ultra-pure Ar gas, mixed with CNTs inside an Ar-filled glovebox, and then ball-milled again for 50 h, in a process very similar to BPC4 as mentioned in **Table 1**.

S1.5. Characterization

High-resolution powder XRD patterns were collected on a Rigaku diffractometer (40 kV, 40 mA) in Bragg-Brentano θ-2θ geometry using a copper Kα radiation (λ = 0.154059 nm). The 2θ step size was 0.01°, and the dwell time per step was 5 seconds. Raman spectra were acquired on a LabRam Aramis (Horiba Jobin Yvon) instrument with an Ar laser source of 532 nm in a macroscopic configuration. Lorentzian fitting was used to calculate the data from Raman analysis. Solid-state ^{13}C and ^{31}P ssMAS-NMR spectra were recorded using a Bruker Avance II 500 spectrometer (125.7 MHz) equipped with a 4-mm diameter solid-state probe head and ZrO_2 rotors rotating at 10 kHz. The spectra were normalized by the mass of each sample. The CW EPR spectra were recorded on a Bruker EMX plus spectrometer in the X band with a liquid He temperature control system (ER4112HV). The spectra were collected with the following experimental parameters and normalized by the mass of each sample: microwave frequency of 9.64 GHz, microwave power of 1 mW, modulation amplitude of 1 G, and modulation frequency of 100 kHz. The experiment was conducted at 4 K to reduce the noise.[1] TG curves were acquired using a TGA/DSC 1 (Mettler Toledo) analyzer, and the samples were placed in alumina pans in air or Ar flow rate of 50 mL min^{-1} at a constant heating rate of 10 K min^{-1}. FT-IR spectroscopy was performed on a Bruker (Model Vertex 70) spectrometer in diffuse reflection mode with a

Spectra Tech Collector II accessory. ToF-SIMS (ToF-SIMS 5 spectrometer, ION-TOF) analysis was performed using a Bi_3^{2+} beam operating at 30 keV with a current of 0.34 pA for the surface. Both positive and negative spectra were acquired in the range of m/z = 0–500 with an analyzed area of 500 μm × 500 μm for surface measurements or 100 μm × 100 μm for depth profiles. A 2000 eV Cs^+ (33.25 nA) beam was used to sputter the cycled samples with a sputtering area of 350 μm × 350 μm.

The water contact angles were also measured to compare the surface hydrophilicity of BP60 samples before and after the controlled air exposure, using the sessile drop technique with a Phoenix 300 Touch (SEO) instrument at ambient temperature and normal air atmosphere. The instrument was equipped with a camera to capture images, and the angles were measured using the SEO software. A water droplet 4–5 μl in volume was used in each measurement. The tests were repeated 5–7 times to ensure reliability of the results, and the averaged θ values were reported. In addition, the surface wetting of $\mathrm{LiPF_6}$ electrolyte on BPC4 composite was investigated to ensure an appropriate wettability.

The Brunauer-Emmett-Teller (BET) surface area was measured by a Quantachrome® ASiQwin™ (Autosorb-iQ 2ST/MP) system with nitrogen adsorption at 77 K. The morphology of the ball-milled samples was evaluated via field emission scanning electron microscopy (FESEM, JEOL-7800F) with energy-dispersive X-ray spectroscopy (EDS) to semi-quantitatively examine the microstructure. The TEM analyses were performed with a spherical aberration correction scanning transmission electron microscope (Cs-corrected-STEM; JEM-ARM 200F, JEOL) working at an acceleration voltage of 200 kV, coupled with EDS and EELS analyses. The EELS measurements were also performed by another FEI Titan™ HRTEM system with an acceleration voltage of 80–300 kV. The sp^2 bonding (C=C bonds fraction) in all the considered counterparts was examined by EELS analysis in an STEM mode of the carbon K near-edge structure using the Equation (S1):[2,3]

$$\mathrm{sp^2\%} = \frac{\frac{I^u_{\pi^*}}{I^u_{\pi^*}+I^u_{\sigma^*}}}{\frac{I^g_{\pi^*}}{I^g_{\pi^*}+I^g_{\sigma^*}}} \tag{S1}$$

where I^u and I^g are the integrated peak intensities of the composites and graphite, respectively. The EELS and Raman results in **Figure 1a** are averaged over 10–15 individual spectra taken from different spots on the samples. The increased errors are related to the increasing inhomogeneity of the results.

For quantitative evaluation of the BP crystalline phase upon milling, the value of V_f was calculated from the XRD profiles. To this end, the integrated areas of the amorphous and crystalline peaks were carefully separated by the peak-fitting software, and the V_f of BP nanocrystals was estimated roughly as follows:[4,5,6]

$$V_f = \frac{A_c}{A_c + A_a} \tag{S2}$$

where A_c and A_a are the total integrated areas of crystalline BP and amorphous RP phases, respectively. The considered 2θ range was 10–75 degrees, divided into three distinct areas (10–20°, 21–44°, and 44-75°), to fully cover the three main amorphous regions of RP in the XRD and compare to the corresponding BP peaks within, as illustrated in **Figure S1**. For instance, the RP (013) and BP (020) peaks were considered in the first range (10–20°) for samples ball-milled for 5–60 h. In the second range, RP ($31\bar{8}$) was compared with four BP peaks, namely (021), (111), (002), and (131). Each ball-milled sample was carefully analyzed, and the exact positions of the XRD peaks were determined by both Lorentzian and Gaussian curve fitting, and found to be in good agreement with each other. However, only the values obtained from Lorentzian curve fitting were taken into account. It is because the V_f values determined from the errors in the Lorentzian function had lower uncertainty than those from the Gaussian function. The error bars are also presented in **Figure S3c**. A reasonable comparison with almost the same results could also be carried out by means of TEM images to distinguish the two amorphous and crystalline phases.

S1.6. Electrochemical tests

For the electrochemical measurements, CR2032 coin-type half cells were assembled with Li or Na metals as the counter electrodes inside the argon-filled glovebox. The electrode mixture contained one of the active materials (BPC1 to BPC5), carbon black as the conductive agent, and binder in a weight ratio of 70:15:15. The binary cross-linked binder was prepared with PAA (3 wt.% in water) and NaCMC (1 wt.% in water) in 1:1 weight ratio. Then, the mixture was doctor-bladed on copper foil with the thickness of 10 μm. Control experiments were also conducted using bare PAA, NaCMC, and PVDF binders (with similar weight ratio of 70:15:15) to compare the performance of electrode materials in LIB. The prepared electrodes were vacuum dried at 150 °C for 2 h. The slurry loading on the electrodes was 1.45–1.65 mg. The electrolyte was 1 M $LiPF_6$ in a mixture of ethylene carbonate, dimethyl carbonate, and diethyl carbonate (EC:DMC:DEC = 2:2:1 by volume) containing fluoroethylene carbonate (FEC, 10 vol.%) for the LIB tests; and 1 M $NaClO_4$ in a mixture of EC:DEC (1:1 by volume) plus 10 vol.% FEC for the NIB experiments. Galvanostatic discharge/charge, CV, and EIS tests were conducted using a Princeton Applied Research VMP2 potentiostat/galvanostat. Charge/discharge tests were carried out in the range of 0.01–2.0 V versus Li/Li^+ or Na/Na^+. CV tests were conducted at a scan rate of 0.1 mV s^{-1} within the range of 0–2.0 V. EIS was carried out by applying a perturbation voltage of 5 mV between 1 Hz and 10^5 Hz.

For post-electrochemistry evaluations, the cells were disassembled inside the glovebox, carefully rinsed with DMC, and then dried in the glovebox.

S2. Additional characterizations and discussions

Figure S1 depicts the XRD patterns of RP after various milling times up to 60 h, and confirms that increasing the milling time results in sharpened, more intense BP peaks. After around 60 h of milling, the BP had a fully crystalline structure with negligible amorphous areas**.**

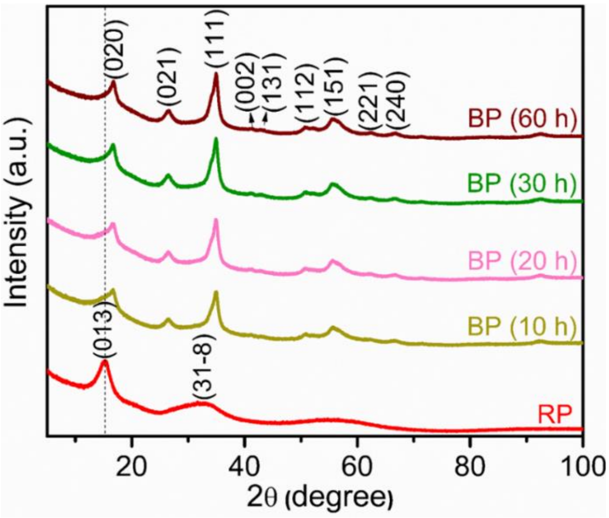

Figure S1. XRD patterns of crystalline BP produced by milling the amorphous RP for various durations.

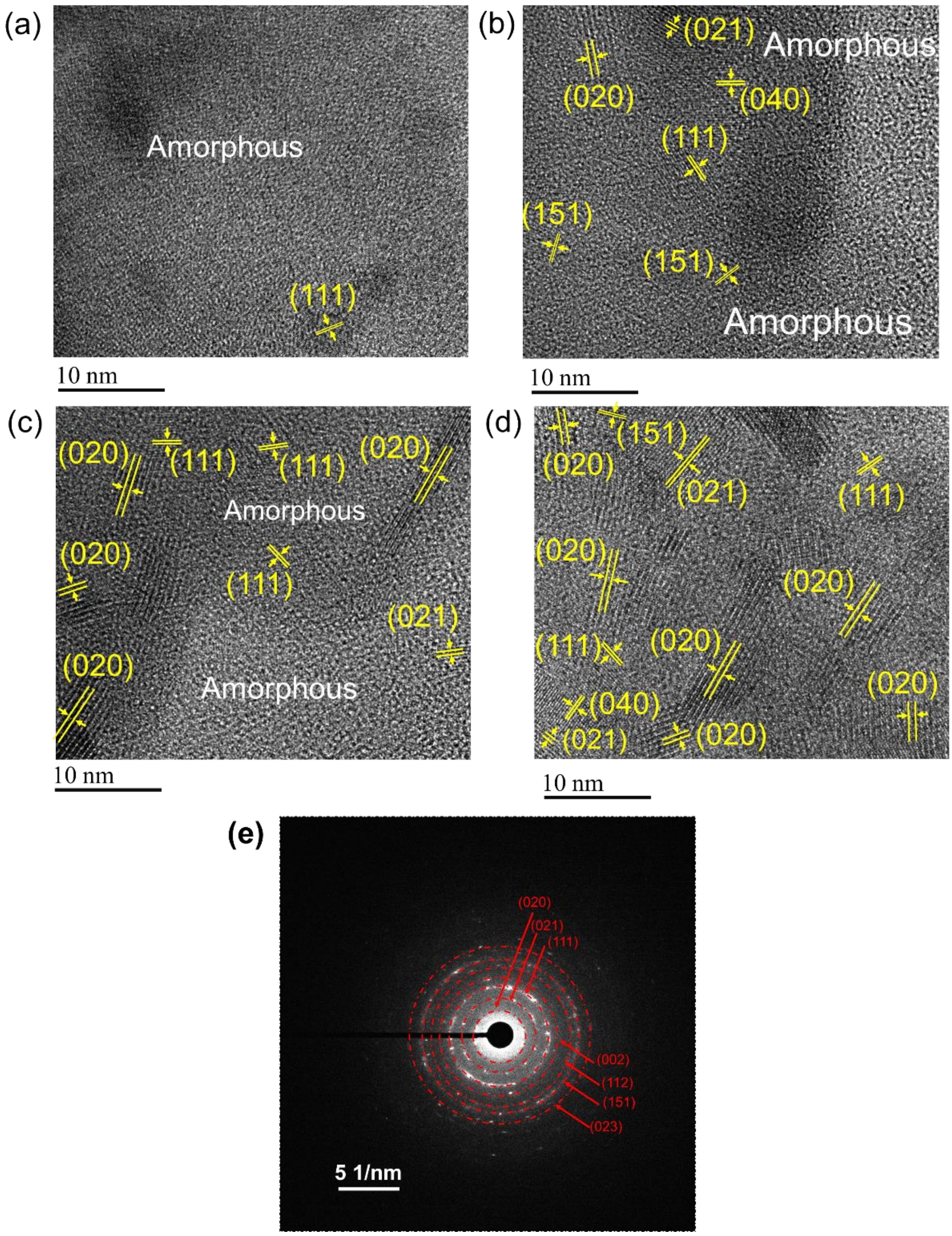

Figure S2. Comparison of the amorphous phase with the crystalline areas in the BP samples as a function of milling time: (a) 10 h, (b) 20 h, (c) 30 h, and (d) 60 h. These results completely confirm the V_f values derived from the XRD results in **Figure S3c**. (e) SAD pattern of BP60, which clearly shows all the important BP rings and thus indicates its fully polycrystalline nature.

Figure S3a presents the XRD patterns of CNT, BP30, BP60, and the composites BPC1 to BPC4 produced through **Scheme 1, approach A**, demonstrating the crystalline nature of the produced composites. Two characteristic CNT peaks at 26° and 43.5° are in accordance with the graphite-3R phase (No. 00-026-1079). The peaks of the milled RP-carbon (RPC) composites (**Figure S3b**) were broadened dramatically when compared to the starting materials (RP and CNTs). This is attributed to the disappearance of medium-range ordered structure of RP and its transformation to a highly disordered amorphous structure in the presence of CNTs. This interesting finding can easily be extended to other BP-based carbon composites, since all previous works of ball-milling RP and carbon materials in one step ended up with the formation of RP-based composites.[7,8,9,10,11,12] It is believed that carbon materials absorb the mechanical energy upon ball milling, which is necessary to overcome the activation energy barrier for the amorphous RP $\rightarrow$ crystalline BP transition. However, in the absence of CNTs, bare BP could be easily synthesized from RP in less than 10 h in this study, as demonstrated in **Figures S1 and S2** through both XRD and TEM analyses. The XRD data were used to determine the content of crystalline BP (V_f) as a function of milling time up to 60 h (**Figure S3c)**. The content of crystalline BP after 5 h of milling was only 12±8%, while this percentage increased to around 94±5% after 60 h, confirming that 60 h was sufficient to reach fully converted, homogeneous BP nanocrystals consistent with ICDD Card No. 01-073-1358. ^{31}P ssMAS-NMR spectroscopy was used to verify the XRD and TEM results. The inset of **Figure S3c** presents a sharp, narrow NMR peak for pure BP at 15 ppm, which is consistent with previous reports.[13,14,15]

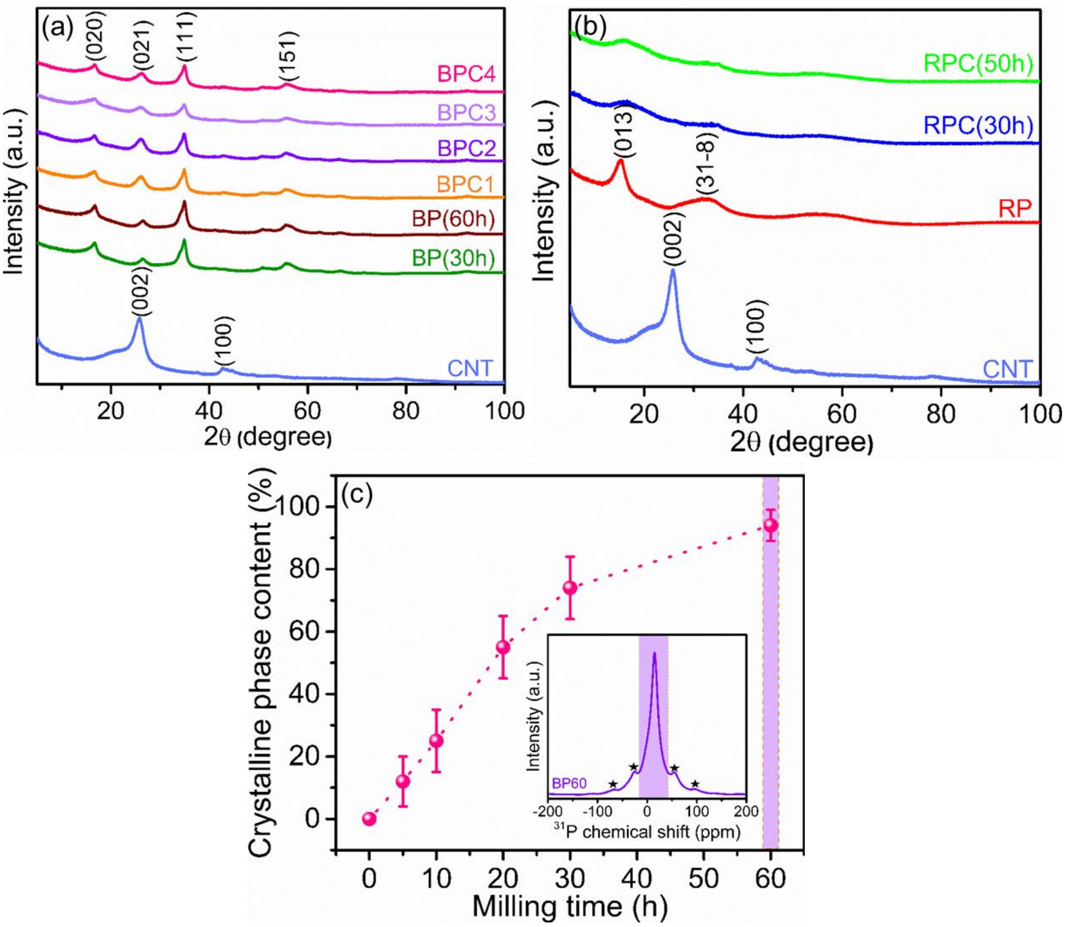

Figure S3. (a) XRD patterns of CNT, BP30, BP60, and four designated BPC composites listed in **Table 1** according to **approach A**. (b) XRD patterns of CNT, RP, and two RPC composites after 30 and 50 h milling, acquired from the one-step ball milling of RP+CNT precursors in **approach B**. The results unambiguously indicate different final products from those obtained using **approach A** (two-step milling). (c) Calculated content of BP crystalline phase versus milling time, based on the XRD patterns. Lorentzian fitting was used to calculate the data from XRD in (c). Inset: ^{31}P ssMAS-NMR spectra of BP60. The sharp peak at 15 ppm confirms the formation of pure BP nanocrystals after 60 h of milling. All spinning sidebands are marked with asterisks (*).

Figure S4a illustrates the morphology of the ball-milled BPC4 powders using SEM analysis, and reveals the presence of irregularly shaped agglomerated particles with a large size distribution from 500 nm to greater than 10 μm. Prolonged milling resulted in more pronounced fraction of ultrafine (nanometer-size) BP particles in BPC4 in comparison with other BPC samples. EDS mapping was further executed to confirm the homogeneous mixture of BP and CNTs upon ball milling. TEM micrographs indicated that the particles are of about 100–500 nm in size. Comparison of the crystallite sizes obtained from the XRD and TEM analyses revealed that the two sets of results have good quantitative correlations. TEM observations, however, showed slightly larger crystallite sizes, which could be attributed to the severe broadening of XRD peaks on account of the formation of BP nanocrystals during milling, as well as the overlapping crystalline and amorphous peaks. Besides, the TEM images in **Figures S4b-g** show that the CNTs covered the BP surface and created a core-shell-like morphology for the BPC4 composite. Both the bright- and dark-field images confirm a strong connection of two components, and demonstrate that sidewall defects and open-ended tips are important in establishing stable connections with the hydrophilic BP particles. Besides, long milling durations only partially disturbed the wall structure and slightly changed the graphitic network, although several non-sp^2 imperfections were formed. These micrographs are completely consistent with the results provided in **Figure 1a**.

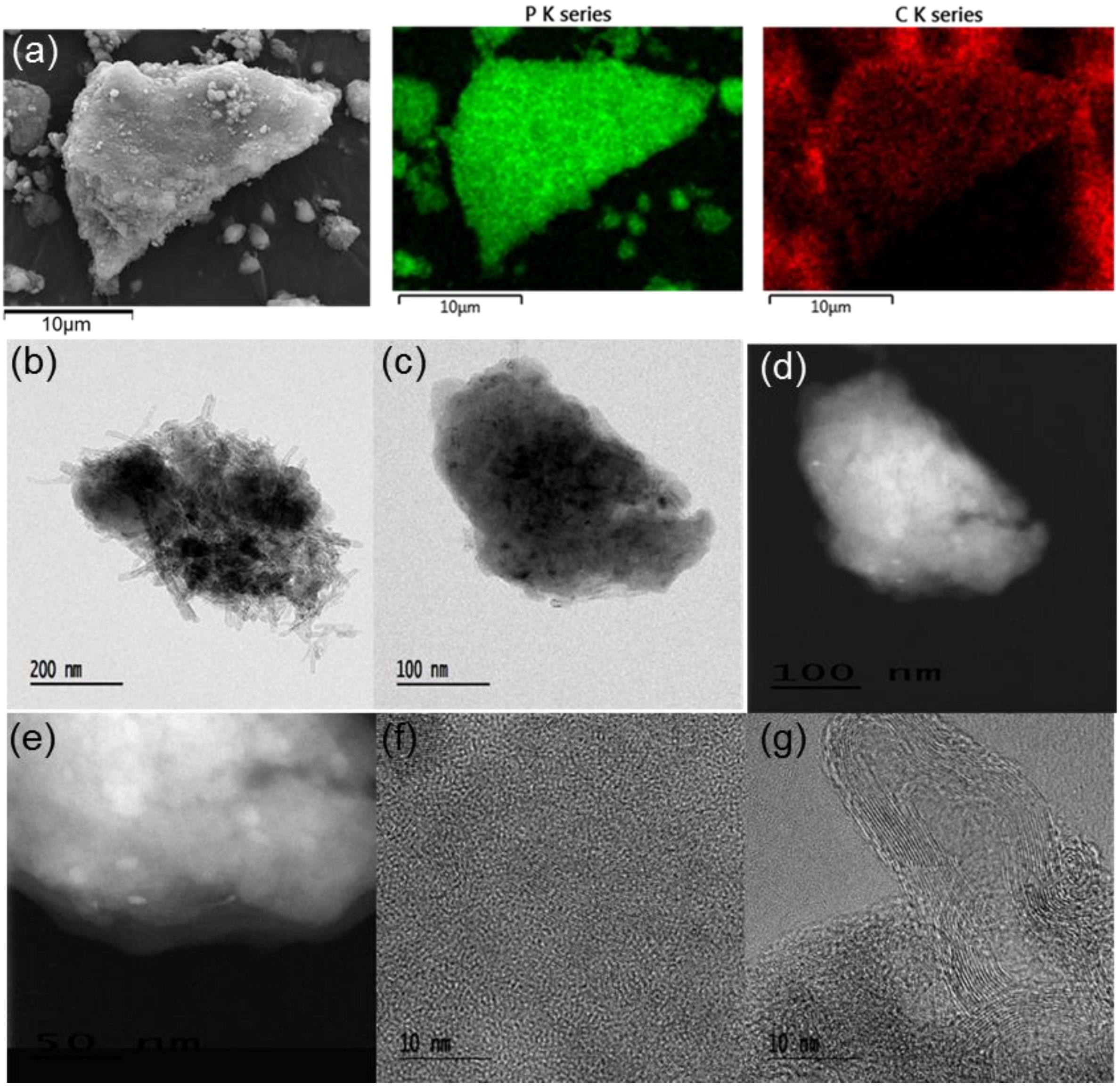

Figure S4. (a) SEM image of a large BPC4 particle, and its elemental mapping results of P and C, showing even distribution of both elements. (b, c) TEM image of BPC4 composite, clearly illustrating a core-shell-like structure with shortened CNTs. (d) Dark-field image of the same particle in (c). (e) High-resolution dark-field image of the BP/CNT interface. (f, g) High-resolution bright field micrographs of the interface.

Figure S5 compares the Raman spectra of RP and BP samples after different milling times. The three Raman active modes of BP near 362, 435, and 465 cm^{-1} are attributed to BP's well-known A_{1g}, B_{2g}, and A_{2g} modes, respectively, and they completely corroborate the XRD results for the formation of BP from RP during ball milling.[14]

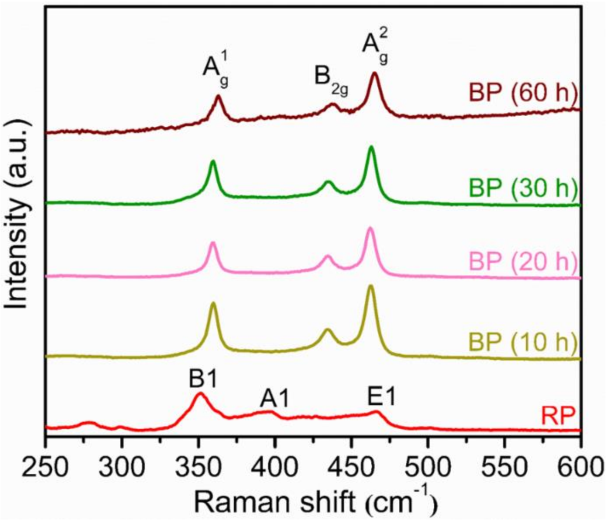

Figure S5. Raman spectra of RP and BP samples after various milling times. The three distinct BP peaks are visible in all ball-milled BP samples.

Figure S6 compares the N_2 adsorption-desorption isotherms at 77 K of BPC3 and BPC4 samples. The isotherms have very similar and characteristic type IV shapes according to the IUPAC classification, with an H_2 hysteresis loop.[16] The size of the hysteresis loop is generally related to the mesopore volume and the connectivity of the pores. The significant N_2 adsorption at low relative pressures indicates the existence of micropores. The specific surface area of BPC4 is 35 m^2 g^{-1}, which is slightly larger than that of BPC3 (26 m^2 g^{-1}). The increased specific surface area might be explained by the opening of the nanotube tips as well as the damaged walls during the milling.

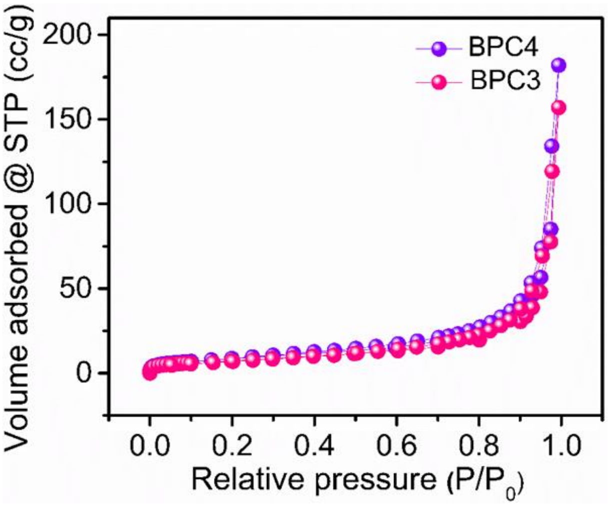

Figure S6. BET surface area comparison of BPC3 and BPC4.

Many researchers have reported the fracturing and shortening of CNTs during the milling process.[17,18,19] CNTs are usually highly curved with few kinks and junctions.[20] High-energy ball milling damages their structural integrity, by weakening the sp^2-type carbons and creating various types of disorders, such as vacancies, adatoms, edges, and interstitials.[18] These structural imperfections are favored for *in situ* interfacial reactions.

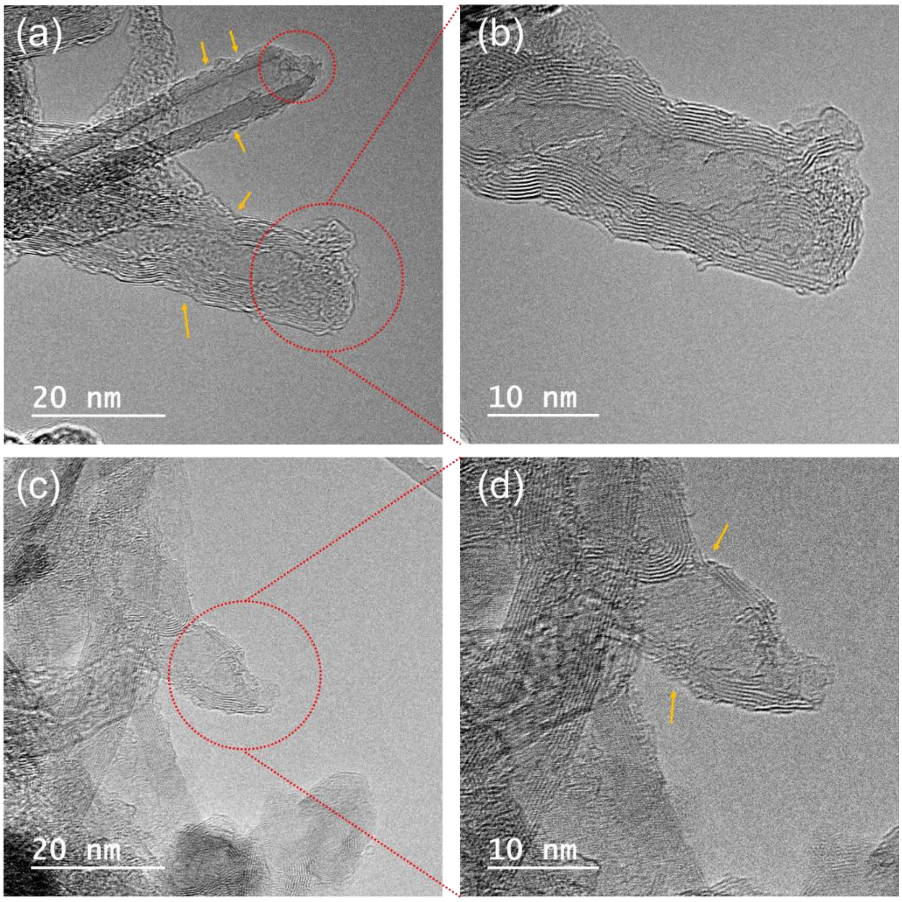

Figure S7. Open-ended CNT tips (red circles) along with several side-wall defects (indicated by orange arrows) in BPC4, which clearly confirm the shortening and functionalization of CNTs after prolonged milling. The d-values remained almost the same, confirming that the graphitization was only slightly affected by the milling, and the structural changes are localized. In addition, H_3PO_4 might be produced from the reaction of water and P_2O_5, thereby partially activating the surface of CNT walls and further enhancing the oxygen functionalities.

As seen in **Figure S8**, the sharp edge at around 286 eV is associated to the 1s→π* transition. This peak is only seen in carbon materials that contain sp^2 bonding.[2,3] Another strong peak at around 293 eV corresponds to the 1s→σ* transition and is detected in all carbon allotropes.[21,22]

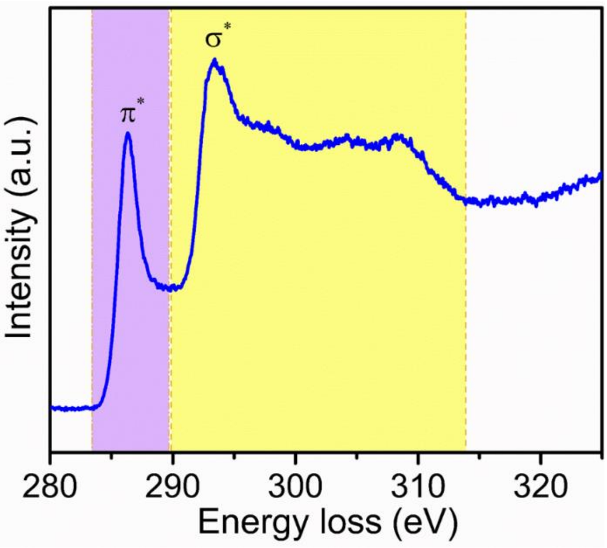

Figure S8. EELS analysis of graphite, which is considered 100% sp^2 carbon.

Recent experimental work as well as theoretical calculations demonstrated that oxygen could spontaneously dissociate on mono- or few-layered phosphorene at ambient conditions.[23,24,25] This exothermic surface oxidation also happens in bulk BP powder to a lesser extent, and it increases exponentially during the first few hours of air exposure as it is energetically favored. Such reactivity between oxygen and BP originates from the sp^3 bonding characteristics of the latter, which provides a lone electron pair on every BP atom.[24] The main reaction product has been established to be phosphorus pentoxide (P_4O_{10} or simply P_2O_5), which exists primarily on the topmost layer of BP.[23]

The TG results (**Figure S9**) also showed an extra 2% weight loss in BPC4-c-NaCMC-PAA in comparison with BPC3-c-NaCMC-PAA, because of the abundant cross links in the former.[26,27]

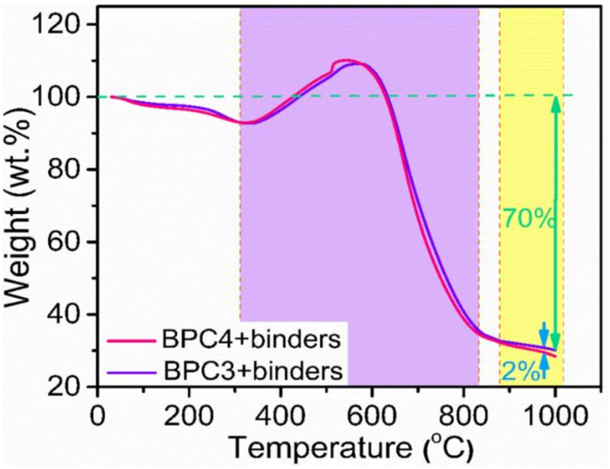

Figure S9. TG curves of BPC3-c-NaCMC-PAA and BPC4-c-NaCMC-PAA.

S3. Additional electrochemical results

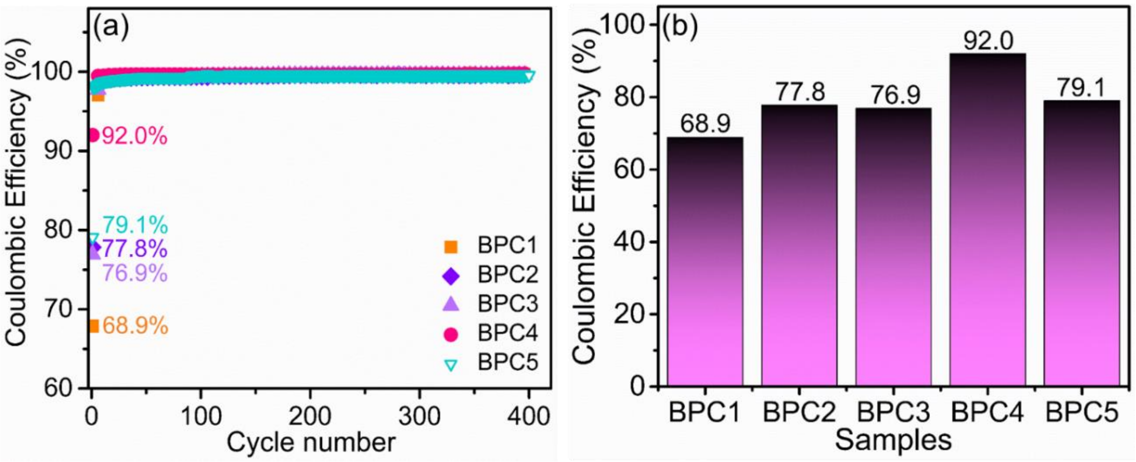

Figure S10. (a) Comparison of CE values of the five composites (BPC1–BPC5) during LIB cyclic tests, confirming the > 92% efficiency of BPC4. (b) Comparison of initial CE values of the five composites. All electrodes were prepared with the c-NaCMC-PAA binder, and the capacity results are based on the mass of BP.

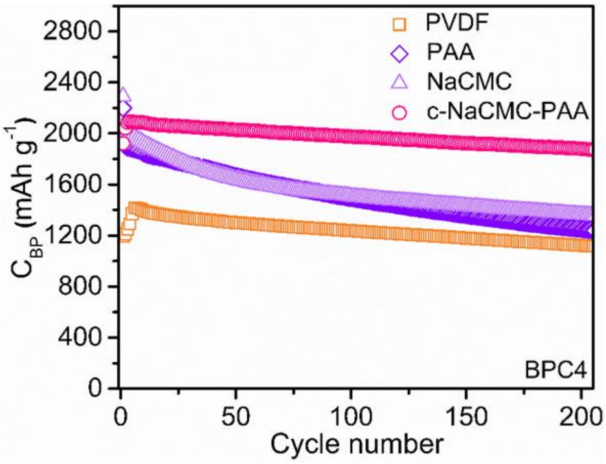

Figure S11. Comparison of cyclic performance of BPC4 up to more than 200 cycles when using various binders: the designated 3D c-NaCMC-PAA, and the alternatives of PAA, NaCMC, and PVDF, all fabricated in a similar weight ratio of 70:15:15 as described above. The results demonstrate the excellent performance of the c-NaCMC-PAA binder.

Table S1. Detailed initial high-rate capacities of the BPC1–BPC5 samples illustrated in **Figure 3f**.

Initial discharge capacity in LIB	**0.2 C**	**0.3 C**	**0.7 C**	**1.5 C**	**2 C**	**3 C**	**4.5 C**	**0.2 C**
BPC1	1100	1435	1251	923	691	539	299	1093
BPC2	1400	1677	1572	1248	1012	794	520	1543
BPC3	1264	1530	1353	1059	831	678	458	1302
BPC4	1950	1862	1751	1644	1588	1518	1346	1713
BPC5	1880	1782	1671	1524	1300	1158	945	1633

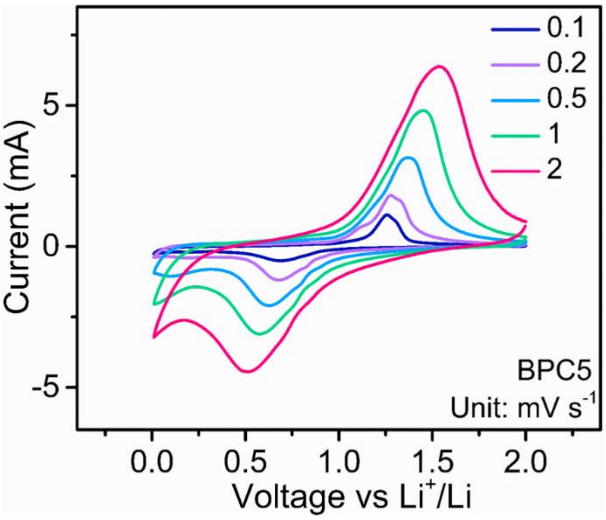

Figure S12. CV curves of BPC5 at different scan rates.

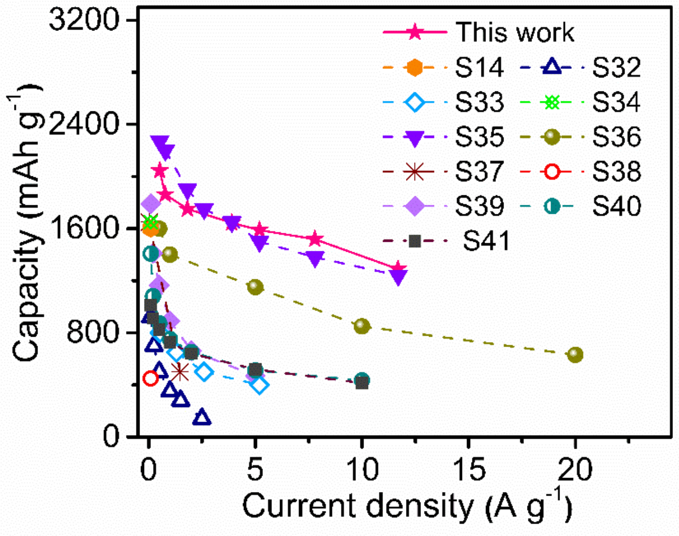

Figure S13. Comparison of the capacities of our target BPC4 with all previous works in LIB at different current densities. Note that the 5th cycle at each current rate was reported in our work and all the references, to better compare the stable capacities.

Figure S14 illustrates the CV curves in the voltage range of 0.01–2.0 V vs. Na/Na$^+$ at 0.1 mV s^{-1} for cycles 1–5. A broad, weak peak appeared at around 0.6 V in the first cathodic scan, due to the formation of the SEI layer.[28,10] A new peak was observed at around 0.9 V in the subsequent scans, likely due to the initial sodiation of BP. Two more cathodic peaks in the range of 0.8–0.01 V centered at around 0.35 and 0.19 V were observed, attributable to Na$^+$ insertion and the formation of Na_xP ($1 < x \leq 3$).[29,30,11] These peaks gradually moved to lower voltage ranges and remained there after five cycles. The potential shift could be explained in terms of the activation step, which also induced a slight increase in the peak intensities from the 3rd to the 5th scans, confirming the progressively improved sodiation kinetics. Peaks located at 0.55, 0.67, and 1.43 V during the first anodic scan also appeared in later scans. These peaks most likely belong to the stepwise Na$^+$ de-insertion from the fully charged Na_3P phase.[10] The current of the peak at 0.67 V was enhanced, and its potential moved to slightly lower voltages from the 1st to the 5th scans, indicating improved desodiation kinetics upon cycling.[31]

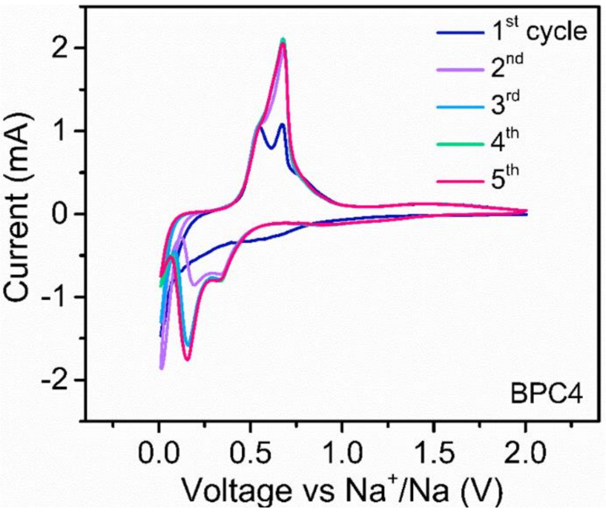

Figure S14. CV curves of BPC4 in the voltage range of 0.01–2.0 V vs. Na/Na$^+$ at 0.1 mV s^{-1} scan rate for the first five cycles.

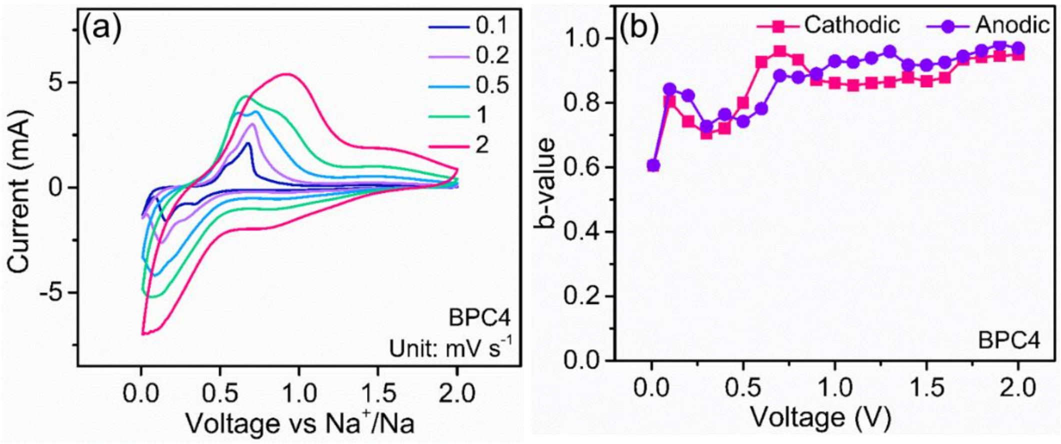

Figure S15. (a) CV curves of BPC4 at different scan rates. (b) Current vs. scan rate of BPC4 at selected constant voltages.

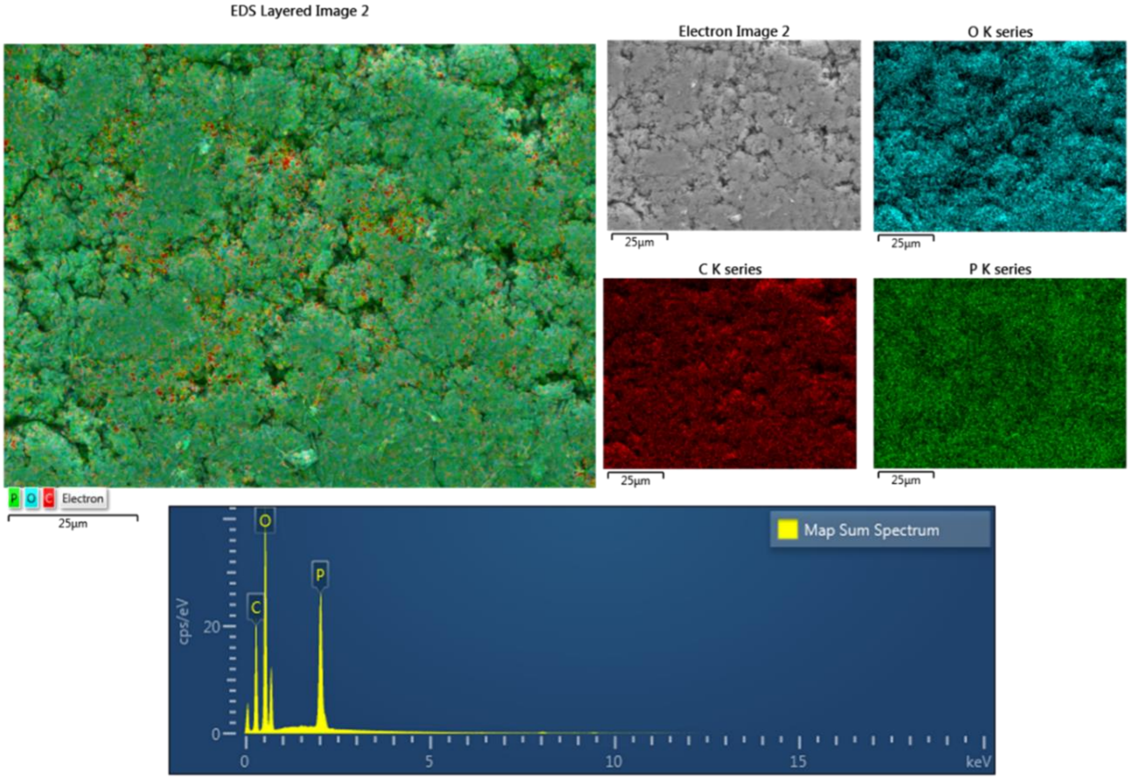

Figure S16. Elemental mapping analysis of P and C in BPC4-c-NaCMC-PAA after 400 cycles in LIB, showing even distribution of both elements.

Table S2. Comparison of electrochemical performance of bulk or 2D nanosheets of BP-based materials for LIB application.

Materials	Highlights	BP:C Ratio	Ref.
BPC4 (BP-MWCNT) (with P-O-C bonds and dehydration cross links)	C_{BP} ~ 1681 mAh g^{-1} after 400 cycles @ 0.2 C (520 mA g^{-1}) (87.5 % retention from the 1st cycle) C_{BP} ~ 1513 mAh g^{-1} after 100 cycles @ 1 C (~ 2600 mA g^{-1}) (83.6 % capacity retention) C_{BP} ~ 903 mAh g^{-1} after 200 cycles @ 4.5 C (~ 11700 mA g^{-1}) (68.1 % capacity retention) Initial CE: 92.0 %	7:3 (wt.%)	**This work**
BP + Graphite	$C_{composite}$ ~ 349 mAh g^{-1} after 50 cycles @ 100 mA g^{-1} (2.0–0.01 V) $C_{composite}$ ~ 700 mAh g^{-1} after 70 cycles @ 100 mA g^{-1} (2.0–0.67 V)	7:3 (wt.%)	[14]
BP nanosheets + graphene	$C_{composite}$ ~ 402 mAh g^{-1} after 500 cycles @ 500 mA g^{-1} (80.2 % retention)	8:2 (wt.%)	[32]
BP	C_{BP} ~ 703 mAh g^{-1} after 60 cycles for RBP[a] @ 50 mA g^{-1} C_{BP} ~ 475 mAh g^{-1} after 60 cycles for WBP[b]@ 50 mA g^{-1}	pure BP	[33]
BP + super P carbon	C ~ 600 mAh g^{-1} after 100 cycles @ 100 mA g^{-1} (2.0–0.78 V)	7:3 (wt.%)	[34]
BP + Graphite	C_{BP} ~1849 mAh g^{-1} after 100 cycles @ 0.2 C (80 % capacity retention from the 2nd cycle)	1:3 (at.%)	[35]
Phosphorus Nanosheets	C ~ 1683 mAh g^{-1} after 100 cycles @ 200 mA g^{-1}	?	[36]
BP +Acetylene black	C ~ 1350 mAh g^{-1} after 30 cycles @ 24 mA g^{-1} (2.5–0.0 V) Initial CE: 89.0 %	8:2 (wt.%)	[37]
BP nanosheets	C_{BP} ~ 432 mAh g^{-1} after 100 cycles @ 100 mA g^{-1} Initial CE: 57.7%	pure BP	[38]
BP quantum dots + N-graphene nanosheets	C ~ 1271 mAh g^{-1} after 100 cycles @ 500 mA g^{-1} C ~ up to 470 mAh g^{-1} after 10 cycles @ 5000 mA g^{-1} Initial CE: 76.8%	66.2% BP	[39]
BP/PEDOT (E-BP/PEDOT)	C ~ 1092 mAh g^{-1} after 100 cycles @ 100 mA g^{-1} Initial CE: 51.0%	90.2 (wt.%)	[40]
Phosphorene–Graphene (PG-SPS)	C ~ 725 mAh g^{-1} after 200 cycles @ 500 mA g^{-1}) (82.4 % capacity retention) C ~ 432 mAh g^{-1} after 800 cycles @ 10000 mA g^{-1} (91.9 % capacity retention) Initial CE: 60.2%	?	[41]

---

[a] BP obtained from red P

[b] BP obtained from white P

Table S3. Comparison of electrochemical performance of bulk or 2D nanosheets of BP-based materials for NIB application.

Materials	Highlights	BP:C Ratio	Ref.
BPC4 (BP-MWCNT) (with P-O-C bonds and dehydration cross links)	C_{BP} ~ 1560 mAh g^{-1} after 200 cycles @ 0.2 C (520 mA g^{-1}) (75.3 % retention from the 1st cycle) C_{BP} ~ 1050 mAh g^{-1} after 100 cycles @ 1 C (~ 2600 mA g^{-1}) (82.7 % capacity retention) C_{BP} ~ 700 mAh g^{-1} after 100 cycles @ 2 C (~ 5190 mA g^{-1}) (82.3 % capacity retention) Initial CE: 87.7 %	7:3 (wt.%)	**This work**
BP + Graphite	$C_{composite}$ ~ 187 mAh g^{-1} after 50 cycles @ 100 mA g^{-1} (2.0–0.01 V) $C_{composite}$ ~ 400 mAh g^{-1} after 100 cycles @ 100 mA g^{-1} (2.0–0.33 V)	7:3 (wt.%)	14
BP/ Ketjenblack-MWCNT	C_{BP} ~ 1826.9 mAh g^{-1} after 50 cycles @ 416 mA g^{-1} (90.8 % capacity retention) C_{BP} ~1700 mAh g^{-1} after 100 cycles @ 1300 mA g^{-1}	7:3 (wt.%)	28
BP+Acetylene black	C_{BP}~ 957 mAh g^{-1} after 23 cycles @ 125 mA g^{-1} @ EC/DEC (1:1) without additive C_{BP}~ 1458 mAh g^{-1} after 23 cycles @ 125 mA g^{-1} @ EC/DEC (1:1) + FEC (5%) C_{BP}~ 1484 mAh g^{-1} after 23 cycles @ 125 mA g^{-1} @ EC/DEC (1:1) + VC (1%)	?	29
Phosphorene+Graphene	$C_{Phosphorene}$~ 2080 mAh g^{-1} after 100 cycles @ 50 mA g^{-1} (85% retention) (1.5–0.0 V)	48.2% BP	42
BP/PEDOT (E-BP/PEDOT)	C ~ 1078 mAh g^{-1} after 100 cycles @ 100 mA g^{-1} Initial CE: 51.5%	90.2% BP	40
BP+ super P carbon black	C_{BP} ~ 1381 mAh g^{-1} after 100 cycles @ 100 mA g^{-1} Initial CE: 62.4% (90.5 % capacity retention from the 1st cycle) (1.5–0.0 V)	7:3 (wt.%)	43

Supporting References

1 S. Wu, G. Chen, N. Y. Kim, K. Ni, W. Zeng, Y. Zhao, Z. Tao, H. Ji, Z. Lee and Y. Zhu, *Small*, 2016, **12**, 2376–2384.

2 Y. Zhu, S. Murali, M. D. Stoller, K. J. Ganesh, W. Cai, P. J. Ferreira, A. Pirkle, R. M. Wallace, K. A. Cychosz, M. Thommes, D. Su, E. A. Stach and R. S. Ruoff, *Science*, 2011, **332**, 1537–1541.

3 P. K. Chu and L. Li, *Mater. Chem. Phys.*, 2006, **96**, 253–277.

4 H. W. Yang, J. Wen, M. X. Quan and J. Q. Wang, *J. Non. Cryst. Solids*, 2009, **355**, 235–238.

5 C. Tan, H. Zhu, T. Kuang, J. Shi, H. Liu and Z. Liu, *J. Alloys Compd.*, 2017, **690**, 108–115.

6 R. S. Maurya, A. Sahu and T. Laha, *Mater. Des.*, 2016, **93**, 96–103.

7 Z. Yu, J. Song, M. L. Gordin, R. Yi, D. Tang and D. Wang, *Adv. Sci.*, 2015, **2**, 1400020.

8 W.-J. Li, S.-L. Chou, J.-Z. Wang, H.-K. Liu and S.-X. Dou, *J. Mater. Chem. A*, 2016, **4**, 505–511.

9 J. Qian, X. Wu, Y. Cao, X. Ai and H. Yang, *Angew. Chemie - Int. Ed.*, 2013, **52**, 4633–4636.

10 J. Song, Z. Yu, M. L. Gordin, S. Hu, R. Yi, D. Tang, T. Walter, M. Regula, D. Choi, X. Li, A. Manivannan and D. Wang, *Nano Lett.*, 2014, **14**, 6329–6335.

11 N. Yabuuchi, Y. Matsuura, T. Ishikawa, S. Kuze, J. Y. Son, Y. T. Cui, H. Oji and S. Komaba, *ChemElectroChem*, 2014, 1, 580–589.

12 Y. Kim, Y. Park, A. Choi, N. Choi, J. Kim, J. Lee, J. H. Ryu, S. M. Oh and K. T. Lee, *Adv. Mater.*, 2013, **25**, 3045–3049.

13 S. Lange, P. Schmidt and T. Nilges, *Inorg. Chem.*, 2007, **46**, 4028–4035.

14 T. Ramireddy, T. Xing, M. M. Rahman, Y. Chen, Q. Dutercq, D. Gunzelmann and A. M. Glushenkov, *J. Mater. Chem. A*, 2015, **3**, 5572–5584.

15 Y. Wang, B. Yang, B. Wan, X. Xi, Z. Zeng, E. Liu, G. Wu, Z. Liu and W. Wang, *2D Mater.*, 2016, **3**, 35025.

16 K. S. W. Sing, D. H. Everett, R. A. W. Haul, L. Moscou, L. A. Pierotti, J. Rouquerol and T. Siemieniewska, *Pure Appl. Chem.*, 1985, **57**, 603–619.

17 N. Rubio, C. Fabbro, M. A. Herrero, A. De La Hoz, M. Meneghetti, J. L. G. Fierro, M. Prato and E. Vázquez, *Small*, 2011, **7**, 665–674.

18 K. S. Munir and C. Wen, *Crit. Rev. Solid State Mater. Sci.*, 2016, **41**, 347–366.

19 N. Pierard, A. Fonseca, Z. Konya, I. Willems, G. Van Tendeloo and J. B. Nagy, *Chem. Phys. Lett.*, 2001, **335**, 1–8.

20 Z. Kónya, J. Zhu, K. Niesz, D. Mehn and I. Kiricsi, *Carbon*, 2004, **42**, 2001–2008.

21 D. Mhamane, V. Aravindan, M.-S. Kim, H.-K. Kim, K. C. Roh, D. Ruan, S. H. Lee, M. Srinivasan and K.-B. Kim, *J. Mater. Chem. A*, 2016, **4**, 5578–5591.

22 Y.-F. Su, J. G. Park, A. Koo, S. Trayner, A. Hao, R. Downes and R. Liang, *Microsc. Microanal.*, 2016, **22**, 666–672.

23 M. T. Edmonds, A. Tadich, A. Carvalho, A. Ziletti, K. M. O’Donnell, S. P. Koenig, D. F. Coker, A. H. Castro Neto and M. S. Fuhrer, *ACS Appl. Mater. Interfaces*, 2015, **7**, 14557–14562.

24 G. Wang, W. J. Slough, R. Pandey and S. P. Karna, *2D Mater.*, 2016, **3**, 25011.

25 Y. Huang, J. Qiao, K. He, S. Bliznakov, E. Sutter, X. Chen, D. Luo, F. Meng, D. Su, J. Decker, W. Ji, R. S. Ruoff and P. Sutter, *Chem. Mater.*, 2016, **28**, 8330–8339.

26 J. Zhang, D. Jiang, H.-X. Peng and F. Qin, *Carbon*, 2013, **63**, 125–132.

27 I.-W. Peter Chen, R. Liang, H. Zhao, B. Wang and C. Zhang, *Nanotechnology*, 2011, **22**, 485708.

28 G.-L. Xu, Z. Chen, G.-M. Zhong, Y. Liu, Y. Yang, T. Ma, Y. Ren, X. Zuo, X.-H. Wu, X. Zhang and K. Amine, *Nano Lett.*, 2016, **16**, 3955−3965.

29 M. Dahbi, N. Yabuuchi, M. Fukunishi, K. Kubota, K. Chihara, K. Tokiwa, X. Yu, H. Ushiyama, K. Yamashita, J.-Y. Son, Y.-T. Cui, H. Oji and S. Komaba, *Chem. Mater.*, 2016, **28**, 1625–1635.

30 W. J. Li, S. L. Chou, J. Z. Wang, H. K. Liu and S. X. Dou, *Nano Lett.*, 2013, 13, 5480–5484.

31 Y. Zhu, Y. Wen, X. Fan, T. Gao, F. Han, C. Luo, S.-C. Liou and C. Wang, *ACS Nano*, 2015, **9**, 3254–3264.

32 L. Chen, G. Zhou, Z. Liu, X. Ma, J. Chen, Z. Zhang, X. Ma, F. Li, H. M. Cheng and W. Ren, *Adv. Mater.*, 2016, **28**, 510–517.

33 L.-Q. Sun, M.-J. Li, K. Sun, S.-H. Yu, R.-S. Wang and H.-M. Xie, *J. Phys. Chem. C*, 2012, **116**, 14772–14779.

34 C.-M. Park and H.-J. Sohn, *Adv. Mater.*, 2007, **19**, 2465–2468.

35 J. Sun, G. Zheng, H.-W. Lee, N. Liu, H. Wang, H. Yao, W. Yang and Y. Cui, *Nano Lett.*, 2014, 14, 4573–4580.

36 Y. Zhang, X. Rui, Y. Tang, Y. Liu, J. Wei, S. Chen, W. R. Leow, W. Li, Y. Liu, J. Deng, B. Ma, Q. Yan and X. Chen, *Adv. Energy Mater.*, 2016, **6**, 1502409.

37 M. Nagao, A. Hayashi and M. Tatsumisago, *J. Power Sources*, 2011, **196**, 6902–6905.

38 G. Zhao, T. Wang, Y. Shao, Y. Wu, B. Huang and X. Hao, *Small*, 2017, **13**, 1602243.

39 L. Pan, X. D. Zhu, K. N. Sun, Y. T. Liu, X. M. Xie and X. Y. Ye, *Nano Energy*, 2016, **30**, 347–354.

40 Y. Zhang, W. Sun, Z.-Z. Luo, Y. Zheng, Z. Yu, D. Zhang, J. Yang, H.-T. Tan, J. Zhu, X. Wang, Q. Yan and S.-X. Dou, *Nano Energy*, 2017, **40**, 576–586.

41 Y. Zhang, H. Wang, Z. Luo, H.-T. Tan, B. Li, S. Sun, Z. Li, Y. Zong, Z. J. Xu, Y.

Yang, K.-A. Khor and Q. Yan, *Adv. Energy Mater.*, 2016, **6**, 1600453.

42 J. Sun, H.-W. Lee, M. Pasta, H. Yuan, G. Zheng, Y. Sun, Y. Li and Y. Cui, *Nat. Nanotechnol.*, 2015, **10**, 980–985.

43 B. Peng, Y. Xu, K. Liu, X. Wang and F. M. Mulder, *ChemElectroChem*, 2017, **4**, 2140–2144.